Article

Angular Mapping of Protein Structure Using Nonlinear Optical Measurements

Bason Clancy,[1,*] Ben Moree,[1] and Joshua Salafsky[1,*]
[1]Biodesy, Inc., South San Francisco, California

ABSTRACT   Proteins are inherently dynamic, flexible molecules that execute precise conformational changes to perform their functions, but existing techniques to directly measure relevant structural changes in solution at room temperature remain limited. Here, we demonstrate a structural technique using second-harmonic generation and two-photon fluorescence under single-laser excitation to map both the mean angular orientation and the distribution width of a probe at various sites throughout the protein with high sensitivity. Our work resolves distinct dihydrofolate reductase (DHFR) ligand-protein conformations, allows interrogation of regions unresolvable by other techniques, and reveals structural differences between DHFR and a point mutant (DHFR-G121V). The technique, angular mapping of protein structure, enables direct and rapid determination of previously unseen aspects of protein structure in a benchtop optical system.

SIGNIFICANCE   We introduce a structural technique, angular mapping of protein structure, which measures the angular orientation (mean angle) and flexibility (distribution width) of a probe at the individual residue level. The technique characterizes protein conformations and conformational changes, providing precise structural information on protein samples in solution using a benchtop optical system. We apply the method to investigate ligand-induced structural changes in dihydrofolate reductase at multiple sites and in regions unresolvable by x-ray crystallography. We also characterize the functionally relevant conformations of dihydrofolate reductase-G121V, a point mutant for which no x-ray structures exist, precisely measuring how a single point mutation changes the protein structure relative to wild-type both near the mutation and at distal, allosteric sites.

INTRODUCTION

High-resolution structural data provides mechanistic insight into the regulation of biological function and informs computational modeling and therapeutics development. Existing structural techniques such as x-ray crystallography (1), nuclear magnetic resonance (NMR) spectroscopy (2), and cryoelectron microscopy (3) have proven invaluable for structural biology, although each technique is subject to specific challenges and limitations. Furthermore, many samples are not amenable to study because of inherent size limitations or intrinsic disorder, and at least in some

cases, crystallization can force proteins into conformations not present in solution (4,5). Given the importance of understanding protein structure in biology, additional techniques to directly and sensitively measure changes in protein structure are needed.

Here, we report a technique for directly probing protein structure at specific, labeled residues using a combination of polarized second-harmonic generation (SHG) and two-photon fluorescence (TPF) measurements. Both SHG and TPF signals are highly dependent on probe angular orientation, making the technique sensitive to angular differences upon ligand binding or between different states of a given protein. The combination of SHG and TPF allows for two measurements, a mean angle (θ_0) and a distribution width (σ), of a probe to be determined relative to the surface normal (Fig. 1, *A* and *B*). SHG and TPF have previously been used together in microscopy to improve imaging by taking advantage of the distinct contrast mechanisms that produce SHG and TPF (6). Various approaches combining
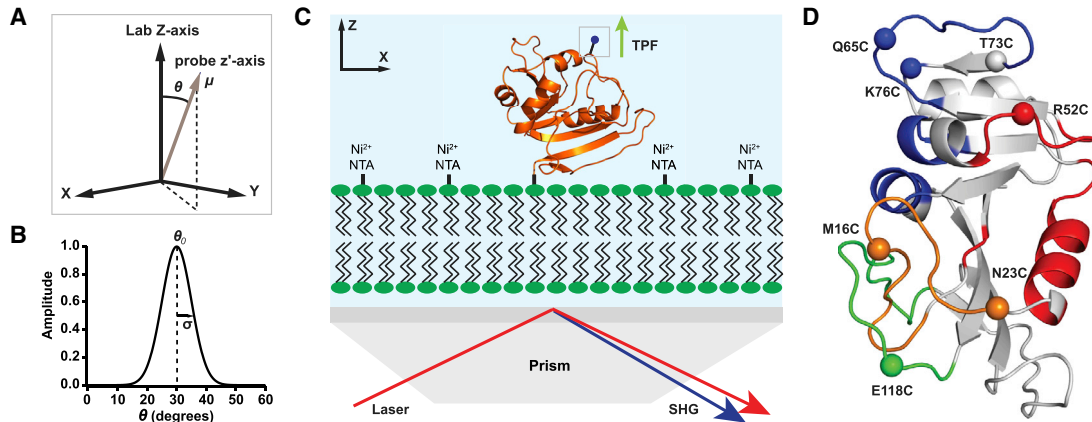
FIGURE 1 Diagram of experimental system and definition of coordinate system. (A) Angular experiments are sensitive to the angle θ between the lab Z axis (*black*) and the probe z' axis (*light brown*), defined by the probe dipole moment, μ. (B) Reported mean angle (θ_0) and Gaussian distribution width (σ) (SD) of the probe dipole moment are shown. (C) Probe-labeled (*boxed*) DHFR (*orange*) is bound to a glass-supported lipid bilayer (*green ovals*) through a His-tag Ni-NTA linkage. An 800-nm beam from a Ti:Sapphire laser (*red*) is directed by a prism to undergo total internal reflection at the glass/water interface. Emitted SHG light (*blue*) is detected after the prism. TPF light (*green arrow*) is collected using a fiber positioned 7.5 mm directly above the sample (not shown). Drawing is not to scale. (D) Shown is a ribbon diagram of the DHFR E:NADPH holoenzyme (Protein Data Bank: 1RX1) with probe locations at engineered cysteines denoted by solid spheres. Colored areas highlight the F-G loop (*green*), Met20 loop (*orange*), co-factor-binding pocket (*blue*), and substrate-binding pocket (*red*).

SHG and absorption techniques have previously been used to characterize θ_0 and σ for probes attached to surfaces (7,8) and at the air-water interface (9). SHG and TPF have also been used in microscopy to image probe-labeled lipid vesicles, yielding θ_0 and σ for the probes embedded in the membrane (10). These previous studies did not measure protein structure or probe angular change in dynamic molecules such as proteins (11), whose inherent flexibility makes determining σ critically important.

Here, we use polarized measurements of SHG and TPF, produced simultaneously, to characterize structure and structural differences of protein molecules attached to a glass-supported lipid bilayer (Fig. 1 C). Angular mapping of protein structure (AMPS) uses low numerical aperture TPF detection (Fig. S1), which allowed us to obtain analytical solutions for the angular parameters (θ_0 and σ). Protein structural changes at interfaces have also been investigated using chiral vibrational sum frequency generation (SFG), a surface-selective nonlinear optical technique similar to SHG (12). Chiral SFG is a label-free way to observe changes in protein secondary structures, such as α-helices and β-sheets, at an interface (13). One shortcoming of chiral SFG is its dependence on secondary structures for signal production, which prohibits obtaining more granular information on protein structure. In contrast, by labeling specific sites throughout the protein AMPS provides residue-level resolution on protein structural change and dynamics.

SHG signals are highly dependent on the polar angle, θ, between the laboratory Z axis and the molecular probe z' axis (Fig. 1 A) (14). In the case considered here of an azimuthally isotropic monolayer of molecules possessing a single-dominant molecular hyperpolarizability along the probe z' axis (8), the probe angular orientation can be related to the ratio, R_{SHG}, of the SHG intensities produced under p- and s-polarized laser excitation (I_{ppp} and I_{pss}, respectively), corrected for background interference (see Materials and Methods). At the critical angle for total internal reflection, R_{SHG} is expressed as follows (15):

$$R_{SHG} = \frac{I_{ppp}}{I_{pss}} = 4\left(\frac{f_z}{f_y}\right)^4 \left(\frac{\langle\cos^3\theta\rangle}{\langle\sin^2\theta\cos\theta\rangle}\right)^2, \qquad (1)$$

where the brackets denote an average over all angular orientations (see Supporting Derivations for more details). A Gaussian distribution function (Fig. 1 B) is assumed when performing the average. The constants f_y and f_z are known factors that modify the electric field on the surface because of Fresnel reflections at the prism front surface and prism-buffer interface (15).

For TPF, both absorption and emission processes depend upon the orientation of the dipole moment, μ, with respect to the surface normal (16). For our probe, μ is parallel to the SHG hyperpolarizability axis (8), and the absorption and emission dipole moments are co-linear (see Fig. S2). Under these conditions, we derived an expression for the ratio of TPF intensities, R_{TPF}, for our low numerical aperture geometry to be as follows:

$$R_{TPF} = \frac{F_{pp}}{F_{ss}} = \frac{8}{3}\left(\frac{f_z}{f_y}\right)^4 \frac{\langle\cos^4\theta\sin^2\theta\rangle}{\langle\sin^6\theta\rangle}, \qquad (2)$$

where F_{pp} and F_{ss} are the TPF intensities for p- and s-polarized laser excitation, respectively (see Supporting Derivations for more details). Eq. 1 for SHG and Eq. 2 for TPF

are used together to uniquely determine the two unknown angular parameters of a probe attached to sites on the protein: the mean angle θ_0 and the width of the Gaussian distribution σ. For the given ratios of SHG and TPF intensities, there exist pairs of values of θ_0 and σ that satisfy each equation alone. A unique solution satisfying both equations is found at the crossing point of the solution pairs (σ, θ_0) for each equation (Fig. S3). Different conformational states and structural differences are mapped using values of σ and θ_0.

To validate our method, we applied AMPS to study distinct ligand-protein complexes of *Escherichia coli* dihydrofolate reductase (DHFR) previously characterized by x-ray and NMR studies. DHFR catalyzes the reduction of dihydrofolate to tetrahydrofolate using nicotinamide adenine dinucleotide phosphate (NADPH) as a cofactor and is a model enzyme for studying protein structure and function. We previously used SHG alone to study ligand-induced conformational changes in DHFR (17). To enable AMPS, proteins must be labeled with a single probe. Therefore, we produced DHFR samples labeled at specific engineered cysteine residues to map probe angles throughout the protein. Sites for cysteine mutagenesis were chosen for their functional relevance and span a range of motion upon ligand binding as observed in x-ray structures. The cysteines were installed in a cysteine-free background (C85A/C152S) (18) and included M16C and N23C in the Met20 active site loop, R52C in the substrate-binding pocket, Q65C and K76C in the cofactor pocket, T73C between the substrate and cofactor pockets, and E118C in the F-G loop (Fig. 1 D). The catalytic activity of each labeled mutant was confirmed to be consistent with wild-type using a solution-based NADPH turnover assay (Fig. S4). To test DHFR binding activity when tethered to a surface, a surface plasmon resonance (SPR) assay was used to measure the binding affinity of trimethoprim (TMP) to DHFR when surface bound via His-tag (Fig. S5). The K_D was unchanged from the value measured in solution, indicating that surface tethering does not impact DHFR activity.

MATERIALS AND METHODS

Protein purification and labeling

All DHFR constructs were prepared and expressed by Biozilla (Biozilla, San Mateo, CA). Briefly, constructs were cloned into a C-terminal 8× His-tagged expression vector under the control of the T7 promoter. Plasmids were transformed in the BL21-DE3 *E. coli* strain, and protein expression was induced with 0.5 mM isopropyl β-D-1-thiogalactopyranoside at an optical density of 0.6–0.7. Bacterial pellets were collected by centrifugation and lysed by freeze-thaw fractionation followed by lysozyme treatment and sonication. Lysed samples were then clarified by centrifugation at $20,000 \times g$ for 30 min at 4°C, and the supernatant was collected and processed using standard Ni-IMAC procedures. After purification, samples were dialyzed into buffer containing 50 mM Tris (pH 7.5), 10% glycerol, and 1 mM 1,4-dithiothreitol. All proteins were purified to at least 90% homogeneity.

Purified DHFR samples were labeled using the Biodesy SHG2-Maleimide dye (1-(2-maleimidylethyl)-4-(5-(4-methoxyphenyl)oxazol-2-yl)pyridinium methanesulfonate) (Biodesy, South San Francisco, CA). This dye has previously been shown through a time-dependent density functional theory calculation to have a single-dominant tensor component along the molecular z′ axis, $\beta_{z'z'z'}$, which is also co-linear with the transition dipole moment (Fig. 1 A) (8). Labeling reactions were performed in 20 mM Tris (pH 7.2), 150 mM NaCl, 0.5 mM tris(2-carboxyethyl)phosphine, and 10% glycerol using either a 3.5× or 5× Molar ratio of dye to protein to target a degree of labeling between 0.5 and 1. All reactions were performed for 90 min on ice and protected from light. Reactions were quenched by rapid desalting using Zeba Spin Columns (Thermo Fisher Scientific, Waltham, MA) equilibrated in storage buffer containing 20 mM Hepes (pH 8.0), 200 mM NaCl, and 10% glycerol. Samples were then aliquoted, snap frozen on liquid nitrogen, and stored at −80°C until ready for use.

NADPH turnover assay

DHFR enzyme assays were measured as previously described (19). Briefly, 0.25 μM of enzyme was mixed with 250 μM of NADPH and allowed to incubate for 5 min. After 5 min, 250 μM of dihydrofolic acid was added to each well, and the change in NADPH absorbance over time at 340 nm was measured using a SpectraMax M2 plate reader (Molecular Devices, San Jose, CA). The amount of NADPH consumed was determined by fitting the change in absorbance to a NADPH standard curve.

SPR assay

SPR studies were conducted by Biosensor Tools (Salt Lake City, UT). Briefly, the experiments were performed at 25°C using a Biacore S51 (GE Healthcare, Uppsala, Sweden) optical biosensor equipped with a Ni-NTA sensor chip and equilibrated with running buffer (25 mM Tris (pH 7.4), 130 mM NaCl, 2.7 mM KCl, 1% DMSO, and 50 μM NADPH). TMP was tested in triplicate in a threefold dilution series using 100 nM as the highest concentration. Responses were fit to a 1:1 interaction model with a mass transport parameter to determine the binding constants. Because the compound dissociated slowly, after each DHFR-capture/TMP-binding cycle, the protein was stripped from the sensor chip using 150 mM phosphoric acid, and a new aliquot of DHFR protein was captured to a density of ~160–180 RU onto the freshly Ni^{2+}-recharged surface.

Experimental setup and data acquisition

Experiments were performed on ultraflat NEXTERION (SCHOTT, Elmsford, NY) glass microscope slides, which have a surface roughness of less than 10 Å, providing a uniform surface for bilayer formation. Slides were prepared by cleaning in a solution of seven parts concentrated sulfuric acid to three parts 30% hydrogen peroxide at 100°C (piranha solution) for 20 min. Slides were then rinsed with purified water and dried with compressed nitrogen. Individual experimental wells were constructed on a slide by attaching a 2-mm thick silicon gasket with an adhesive backing patterned with 16 individual 3-mm diameter circular cutouts (Fig. S1). Ni-NTA lipid bilayers were deposited on the bottom of each well by injecting a solution of lipid vesicles (10 μL) and incubating for 30 min. After incubation, excess lipids were removed by 10 washes of 25 nM Tris (pH 7.4), 150 mM NaCl, and 2.7 mM KCl (Tris-buffered saline buffer) with or without either 100 μM NADPH or NADP+ (assay buffer), depending on the experiment. Protein in assay buffer was then added to each well at a final concentration of 1 μM and incubated overnight at 4°C. Immediately before data was acquired, excess protein still in solution and not tethered to the lipid bilayer was removed using 10 washes of assay buffer. Folate experiments were performed by injecting folate at a final

concentration of 500 μM into wells already containing bilayer-tethered protein.

Our optical setup is detailed in Fig. S1. Briefly, a beam from an 800 nm Mai Tai Ti:Sapphire laser (Spectra-Physics, Santa Clara, CA) with an average power of ~400 mW pulsed at ~80 fs with a repetition rate of 80 MHz was focused using a 100 mm lens onto the bottom of a sample well. The polarization of the beam was controlled using a 10RP02-46 zero-order half-wave plate (Newport, Irvine, CA) mounted on a PRM1Z8 precision motorized rotation stage (Thorlabs, Newton, NJ). Data was acquired by recording photon counts for SHG and TPF in two separate H8259 photomultiplier tubes (PMTs) (Hamamatsu, Bridgewater, NJ). Low numerical aperture TPF detection was accomplished using a custom fiber (Fiberguide Industries, Stirling, NJ) with a diameter of 1 mm placed 7.5 mm away from the sample. Experiments were performed in a darkened room with potential background sources removed by FESH0600 and FESH0650 short-pass filters (Thorlabs) placed in front of the TPF PMT and a FF01-375/110 bandpass filter (Semrock, Rochester, NY) along with a FF01-424/SP short-pass filter (Semrock) placed in front of the SHG PMT. These filters isolate the relatively narrow spectrum for SHG (20) and the large Stokes-shifted fluorescence signals (11). A GLB10-405 Glan prism (Thorlabs) oriented to only allow p-polarized light to pass was also placed in front of the SHG PMT. Median SHG and TPF signals for each individual sample well were generated by scanning the excitation laser across the well to obtain 11 individual data points, with a PMT integration time of 50 ms for each point. The median of the 11 data points was used instead of the average to filter out any especially large or small signals due to irregularities in the well. Individual well median values for experimental replicates were averaged, and the average and SD of the replicates were reported in the text. Laser scans were performed once for each polarization. An initial scan was done in s-polarization in each well, the laser beam was then rotated to p-polarization using a half-wave plate, and a second scan of each well was conducted.

SHG background subtraction procedure

SHG intensities were reported with background SHG sources removed. SHG signals are coherent, resulting in wave interference between probe and background signals. Most background SHG originates from water molecules polarized near the glass surface, which have a weak nonlinear susceptibility (21). Background subtraction procedures must take into account the coherent nature of second-harmonic radiation (22). To subtract the unwanted coherent background from the signal of interest (SHG-active probe on the protein), the phase difference between the two sources must first be determined. SHG from background sources, SHG_B, interferes with the protein signal, SHG_P, according to the following:

$$SHG_{tot} = SHG_B + SHG_P + 2\sqrt{SHG_B}\sqrt{SHG_P}\cos\Delta\varphi, \quad (3)$$

where SHG_{tot} is the total signal measured during an experiment, and $\Delta\varphi$ is the phase difference between SHG_B and SHG_P. To determine the desired SHG_P signal in the absence of the background, the above equation is re-arranged to yield the following:

$$SHG_P = SHG_B\left(\cos\Delta\varphi \pm \sqrt{SHG_{tot}/SHG_B - \sin^2\Delta\varphi}\right)^2. \quad (4)$$

To extract the protein-only signal, SHG_P, from the total signal, SHG_{tot}, $\Delta\varphi$ must be determined. The phase can be obtained by modulating the density of labeled protein on the surface and using the fact that SHG and TPF signals scale differently with labeled protein surface number density (molecules/area). The SHG signal is proportional to the square of the labeled protein density on the surface: $SHG_P \propto N^2$, where N is the labeled protein surface density. In contrast, the TPF signal is linearly proportional to the labeled protein density on the surface: $TPF \propto N$. Therefore, the SHG signal can be written as a function of the TPF signal as follows:

$$SHG_P = C_1 TPF^2, \quad (5)$$

where C_1 is an unknown constant acting as a scaling factor between the SHG and TPF signals. Combining Eqs. 3 and 5 yields the following:

$$SHG_{tot} = SHG_B + \left(2\sqrt{SHG_B}\sqrt{C_1}\cos\Delta\varphi\right)TPF$$
$$+ C_1 TPF^2. \quad (6)$$

By performing experiments with surfaces consisting of different ratios of labeled to unlabeled protein, Eq. 6 can be used as a fitting function (Fig. 2) to extract SHG_B, C_1, and $\Delta\varphi$. The expected shape of the curve will resemble a polynomial with constant, linear, and quadratic terms. In the case of no interference ($\Delta\varphi = 90°$), the curve is purely quadratic with an offset given by SHG_B. Destructively interfering signals will dip below SHG_B (Fig. 2 A) at lower concentrations of labeled protein, whereas constructively interfering signals will monotonically increase (Fig. 2 B). Data points used to generate curves were taken at 100% labeled and 100% unlabeled protein (SHG_B) with intermediate concentrations of 2/3, 4/9, 8/27, 16/81, 32/243, and 64/729 (labeled/total).

Phases were determined separately for each single-cysteine mutant and varied depending upon dye attachment site on the protein. To perform SHG background subtraction correctly, it is crucial to determine whether the interference between the background and the probe is constructive or destructive. The magnitude of SHG intensities are symmetric with respect to the surface plane: probe angles of θ and $180° - \theta$ produce identical signals. A $180°$ phase shift between these two signals produces, in our particular system, destructive interference when the dipole moment of the dye points into the upper-half plane (toward the bulk) and constructive interference when the dipole points into the lower-half plane (toward the bilayer). These assignments were used when determining the angles reported in Tables S1 and S2. Phases measured for the single-cysteine mutants varied between 59 and 130°.

Data processing

Each experiment involved calculating angular parameters (mean angle θ_0 and distribution width σ) from individual sample well intensity measurements. The SHG background was removed from the p- and s-polarized SHG signals using the procedure described above. For each 16-well microscope slide, the average of six wells containing unlabeled protein were used to determine SHG and TPF background signal magnitudes for background subtraction. The TPF background, which is incoherent and due to a small amount of ambient light, typically ~1% of the total signal, was removed using direct subtraction. After background subtraction, SHG and TPF polarization ratios (R_{SHG} and R_{TPF}, respectively) for an individual well were then calculated to determine θ_0 and σ within that well. The values of θ_0 and σ reported in the main text are the average and SD of θ_0 and σ across all replicate experimental wells.

Probes attached to the protein are not in a narrowly oriented distribution, requiring two orthogonal techniques to determine θ_0 and σ uniquely. Pairs of θ_0 and σ that satisfy Eqs. 1 and 2 can be found by rearranging those equations to read as follows:

$$\frac{\langle\cos^3\theta\rangle}{\langle\cos\theta\rangle} = \frac{1}{1 + \frac{2}{\sqrt{R_{SHG}}}\left(\frac{f_z}{f_y}\right)^2}, \quad (7)$$
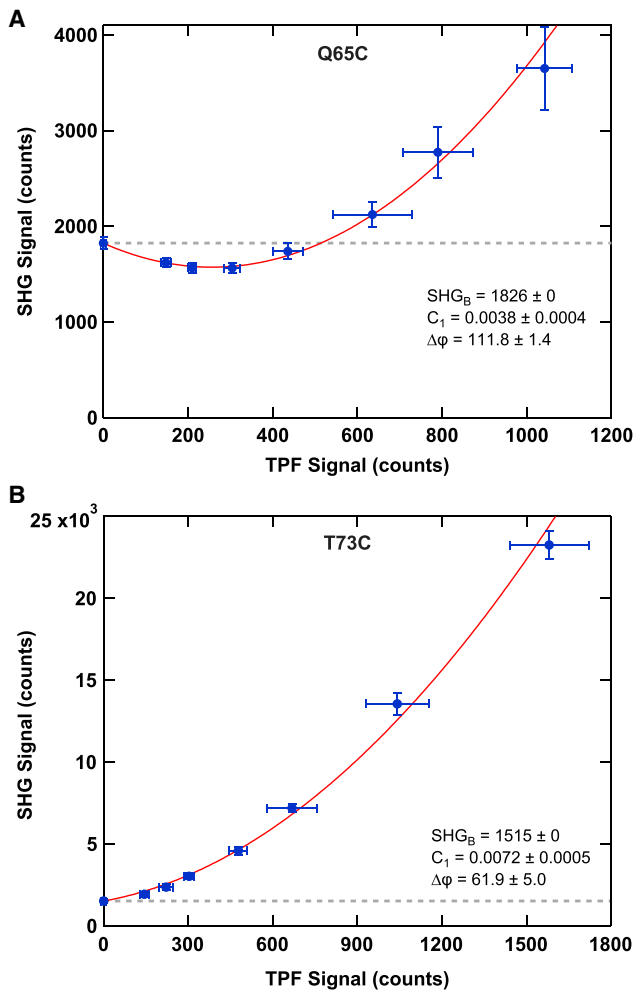
FIGURE 2 Measuring phase differences between background SHG sources and the probe SHG signal. Experimental data (*blue circles*) and theoretical curve fit (*solid red curve*) are used to measure the phase difference for p-polarized laser excitation at probe sites (*A*) Q65C and (*B*) T73C in the presence of NADPH (E:NADPH). Data was collected by varying the ratio of labeled to unlabeled protein, which modulates SHG and TPF signal magnitudes while maintaining a constant protein surface density. Data were fit using Eq. 6 with the background SHG value, SHG_B, fixed to the 100% unlabeled value (*gray dashed line*). SHG and TPF signals are reported in photon counts per 50 ms PMT integration time, and error bars represent SD ($n = 4$ replicates). (*A*) The SHG signal from the Q65C probe site destructively interferes with the SHG background, demonstrating an initial decrease in SHG signal magnitude before reaching a minimum and eventually rising above SHG_B as the labeled protein concentration increases on the surface. These data yielded a phase measurement of $\Delta\varphi = 111.8 \pm 1.4°$. (*B*) The SHG signal from the T73C probe site constructively interferes with the SHG background, displaying a monotonically increasing SHG signal. These data yielded a phase measurement of $\Delta\varphi = 61.9 \pm 5.0°$.

$$\frac{\langle \cos^4\theta \sin^2\theta \rangle}{\langle \sin^6\theta \rangle} = \frac{3}{8}\left(\frac{f_y}{f_z}\right)^4 R_{TPF}. \tag{8}$$

The left-hand side of these equations contains only angular terms, whereas the right-hand side is simply a number that depends upon the measured SHG and TPF ratios. For each equation, there are numerous pairs

of θ_0 and σ that will lead to a correct solution (Fig. S3). To rapidly evaluate these possibilities, a table of solutions for each equation was constructed by evaluating the integrals on the left-hand side of Eqs. 7 and 8. Solutions were evaluated for θ_0 values between 0 and 90° at intervals of 0.1° and for σ values between 0 and 70° at intervals of 0.1°. An algorithm was developed to search through each table to identify θ_0 and σ pairs that correspond to the values on the right-hand side of Eqs. 7 and 8. Linear interpolation was used to find solutions between the 0.1° steps. After the two sets of θ_0 and σ pairs were found, a second algorithm was used to find the common θ_0 and σ pair between the SHG and TPF data sets.

The integrals in Eqs. 7 and 8 were evaluated assuming that the probability density function (PDF) of the angular distribution is Gaussian:

$$P(\theta) = \frac{1}{\sqrt{2\pi}\sigma}e^{-\frac{(\theta-\theta_0)^2}{2\sigma^2}}. \tag{9}$$

A Gaussian distribution was assumed for the PDF because it is the most commonly used (7–10,23–25) and physically reasonable function constructed of only two parameters, θ_0 and σ, the maximal number of parameters our technique can solve uniquely. The Gaussian function has values between $-\infty$ and ∞, but the angle θ is limited to angles between 0 and 180°. Therefore, a wrapped Gaussian is used instead by folding all the contributions into the interval between 0 and 180° when performing the integrals (23). Taking this into account modifies the PDF as follows:

$$\tilde{P}(\theta) = \sum_{n=-\infty}^{\infty} P(2\pi n + \theta) + P(2\pi n - \theta). \tag{10}$$

The sum was evaluated from $n = -2$ to 2, which accurately reconstructs the Gaussian distribution for σ values between up to 70° (23). Integrals were evaluated with a $\sin\theta$ weighting function, leading to averages defined as follows:

$$\langle x \rangle = \frac{\int_0^\pi \tilde{P}(\theta)x\sin\theta d\theta}{\int_0^\pi \tilde{P}(\theta)\sin\theta d\theta}. \tag{11}$$

The width of the angular distribution, σ, is influenced by many factors, including the maleimide linkage between the probe and the protein, the His-tag Ni-NTA linkage between the protein and the lipid bilayer, and the conformational flexibility of the protein. Although it is difficult to separate these contributions to the total σ, it is assumed that changes in σ at individual probe sites due to binding ligands or mutagenesis are only due to local changes in protein flexibility and not due to a change in compliance of the linkages.

RESULTS AND DISCUSSION

AMPS can resolve distinct protein structural states

We first investigated whether the θ_0 and σ measurements can be used to distinguish previously determined conformational states in DHFR. The Met20 loop of DHFR alternates between two conformations, termed occluded and closed, as the enzyme proceeds through its catalytic cycle (Fig. S6) (4). Binding of particular cofactors or substrates dictate the conformation adopted, and a large structural change has been observed for the Met20 loop in x-ray crystal structures between the occluded and closed conformations (Fig. 3 A) (4). We resolved this structural change by creating
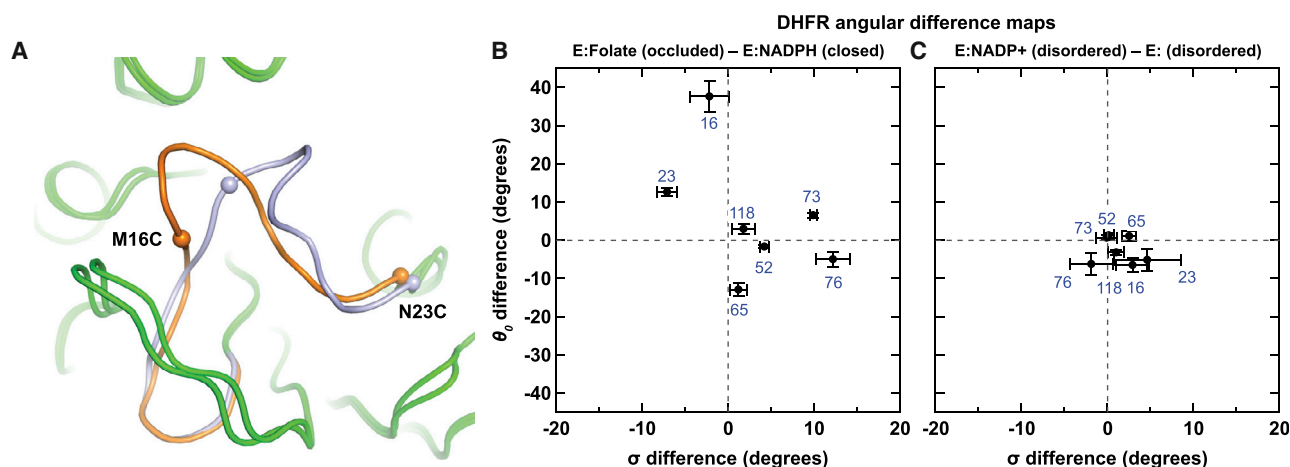
FIGURE 3 Angular differences between DHFR conformational states. (A) X-ray crystal structure overlay highlights the differences in the Met20 loop between the DHFR E:NADPH closed (*orange*, Protein Data Bank: 1RX1) and the DHFR E:Folate occluded states (*blue*, Protein Data Bank: 1RX7). (B) Shown is an angular difference map for DHFR E:Folate − E:NADPH (occluded − closed) at all the sites studied. Error bars represent SD (n = 10 to 20 replicates). (C) Shown is an angular difference map for the DHFR E:NADP+ (disordered) − E: (disordered) states. Error bars represent SD (n = 7 to 28 replicates).

an angular difference map between folate-bound (E:Folate, occluded) and NADPH-bound (E:NADPH, closed) states of DHFR (Fig. 3 B). The largest angular rotation across all the cysteine sites occurred at M16C site on the Met20 loop (37.6 ± 4.1°, Table S1). The N23C site, also located on the Met20 loop, although not a part of the more mobile section of residues 15–21 (26), undergoes a smaller rotation of 12.8 ± 0.9°. Both solution-based AMPS measurements on the Met20 loop confirm the conformational changes seen in x-ray crystallography.

Although the predominant angular difference between the closed and occluded states occurred in the Met20 loop, allosteric perturbations distal to the loop were also observed by AMPS. Experimental and theoretical studies have demonstrated that long-range structural changes can be transmitted through the DHFR structure via networks of amino acids (27–29). The largest network found in DHFR connects the F-G loop to the cofactor-binding pocket, spanning >23 Å (30). In accordance with these observations, we measured a mean angle difference of 12.9 ± 1.2° between the closed and occluded states at the Q65C probe site in the cofactor pocket, over 15 Å from where folate binds in the active site (Fig. 3 B). This allosteric effect is also observed in NMR backbone amide ^{15}N chemical shift data, in which Q65 exhibits a large chemical shift between the NADPH-bound and folate-bound complexes (31).

Angles can be measured using AMPS in unresolved regions of x-ray crystal structures

We also examined a third conformation outside the DHFR catalytic cycle, referred to as "disordered" because of a lack of electron density in x-ray crystal structures for some residues in the Met20 loop, including M16. Although

the region is unresolvable in both the E: apo and some E:NADP+ complexes by crystallography, we determined angular information for M16C using AMPS. Upon comparing angular measurements between the disordered E:NADP+ complex and disordered E: apo protein, which should adopt similar conformations based on heteronuclear single quantum coherence (HSQC) NMR spectra (32), we found minimal angular differences (all ≤6.4°) (Fig. 3 C), revealing that the Met20 loop occupies a similar conformation in both the E:NADP+ complex and the E: apo protein.

The G121V point mutation perturbs the conformation of the active site Met20 loop

We next investigated structural changes in DHFR due to mutagenesis. Point mutations often cause both local and global structural changes that profoundly impact protein function, but their effects remain challenging to identify and study. The G121V mutation on the F-G loop in *E. coli* DHFR impairs the catalytic activity of the enzyme, reducing the rate of hydride transfer by 200-fold (33). Structural perturbations of the mutation have been studied by chemical shift NMR (HSQC) (32), relaxation NMR techniques (29), and molecular dynamics simulations (34). However, x-ray crystal structures of the mutant do not exist.

The observed reduction in catalytic activity of the mutant enzyme suggests a structural change should be found in the active site and the Met20 loop in DHFR-G121V compared with DHFR. Our angular measurements indeed indicated a markedly different conformation at the active site loop M16C site between DHFR and DHFR-G121V for all ligands tested (Fig. 4 A). Moreover, the θ_0 values at M16C for DHFR-G121V did not correspond to either the DHFR closed (E:NADPH) or occluded (E:Folate) states, implying
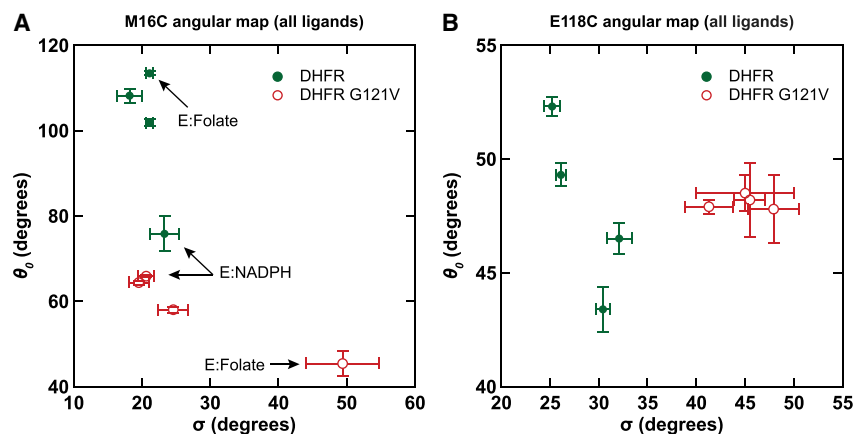
FIGURE 4 DHFR and DHFR-G121V angular maps. Shown are the mean angle and distribution width for apo, NADPH, NADP+, and folate complexes at the M16C (A) and E118C (B) sites for DHFR (green, solid) and DHFR-G121V (red, open). (A) The M16C site exhibits large θ_0 differences between DHFR and DHFR-G121V. θ_0 values for DHFR-G121V indicate a conformation distinct from the DHFR closed (E:NADPH) and occluded (E:Folate) states. Error bars represent SD ($n = 10$ to 20 replicates). (B) Marked increases in σ between DHFR and DHFR-G121V are observed at the E118C site for all ligands, indicating an increase in the flexibility of the F-G loop close to the mutation site. Error bars represent SD ($n = 7$ to 20 replicates).

a distinct conformation. The E:Folate complex, an analog of the tetrahydrofolate product complex in the catalytic cycle (Fig. S6), exhibited the most pronounced angular difference at M16C with a θ_0 change of $68.0 \pm 2.9°$ and an increase in σ by $28.3 \pm 5.3°$ (Tables S1 and S2). These results provide direct structural evidence of the significant perturbation of the catalytically important Met20 loop across all DHFR conformational states as a result of the G121V mutation.

The G121V mutation increases the flexibility of the F-G loop

We also observed significant angular differences between DHFR and DHFR-G121V for all liganded states at the E118C site on the F-G loop near the mutation site. Unfolding molecular dynamics simulations predict that the F-G loop should be significantly more disordered in G121V than in wild-type DHFR in the closed state because of reduced hydrogen bonding with the Met20 loop (34). The increased disorder presumably contributes to the enzyme's impaired function, but direct experimental evidence for this prediction

has not previously been available. Here, we observed pronounced increases in the distribution width (σ) of DHFR-G121V relative to DHFR at E118C in every state with increases of $12.9 \pm 5.2°$ (E:Folate), $15.1 \pm 1.7°$ (E:NADPH), $15.2 \pm 2.5°$ (E:NADP+), and $22.7 \pm 2.7°$ (E:) (Fig. 4 B). However, increased disorder was not observed at the T73C site (average decrease of $4.5 \pm 2.6°$), indicating the increased σ at E118C was a local rather than global effect.

Structural differences throughout the protein can be mapped using AMPS

Finally, we examined structural differences between DHFR and DHFR-G121V across all probe sites for the E:NADPH state. Previous studies by HSQC NMR of E:NADPH complexes indicated that although the Met20 loop for wild-type DHFR adopts the closed conformation, in DHFR-G121V, it is predominantly in the occluded conformation (32). As seen in the E:NADPH difference map and model, structural changes due to the mutation occurred throughout the protein (Fig. 5, A and B). Angular
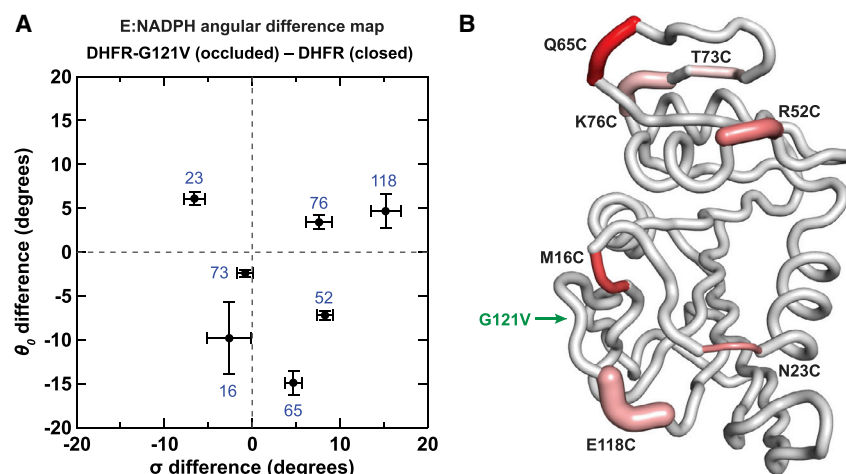
FIGURE 5 DHFR and DHFR-G121V angular differences and model. (A) Shown is an angular difference map between DHFR and DHFR-G121V for the E:NADPH holoenzyme. Pronounced differences occur at the M16C, Q65C, and E118C sites. Error bars represent SD ($n = 9$–20 replicates). (B) Shown is the tube representation of the data in (A) in which relative tube thickness represents σ differences, and darker shades of red indicate larger absolute θ_0 differences. The angular model is overlaid on the DHFR E:NADPH structure (Protein Data Bank: 1RX1), and highlighted areas include the probe sites and immediately adjacent residues. The G121V mutation site is indicated by a green arrow.

differences between DHFR and the DHFR-G121V mutant are observed as expected at the M16C and N23C sites in the Met20 loop, but the largest angular change was observed distally at the Q65C site. Although the M16C site adopts a conformation distinct from the closed or occluded states, the mean angle and angular distribution at the Q65C site for E:NADPH DHFR-G121V ($\theta_0 = 47.4 \pm 0.7°$, $\sigma = 33.6 \pm 0.7°$) is similar to that of the occluded E:Folate complex for DHFR ($\theta_0 = 49.4 \pm 1.0°$, $\sigma = 30.1 \pm 0.6°$) (Tables S1 and S2). In addition to Q65C, allosteric structural perturbations are also found in the cofactor pocket at the K76C and R52C sites. These results provide direct structural confirmation of an allosteric perturbation in the cofactor pocket, which has been indicated by relaxation NMR to be connected to the F-G loop by a network of amino acids (29,30). Taken together, our angular measurements lead us to conclude that the G121V mutation specifically increases the structural flexibility of the F-G loop, which causes allosteric perturbations in both the Met20 loop and the cofactor pocket with the combined effect of severely diminishing the enzyme's activity.

CONCLUSIONS

As compared to x-ray crystallography and NMR spectroscopy, the relative simplicity of AMPS provides structural information using a benchtop optical system. The technique can be used with proteins of any size, and each measurement requires only nanograms of material, is performed in solution at room temperature, and is amenable to a high-throughput implementation. The distribution width (σ) reported by the technique provides unique information on protein structural flexibility, enabling solution-based measurements of regions critical for function that may not be visible by crystallography or for proteins for which no crystal structures are available. We view AMPS as complementary to crystallography and NMR spectroscopy, providing high-resolution structural information on multiple sites, ligands, and mutations, facilitating ligand discovery, protein engineering, and studies of protein structure and function.

SUPPORTING MATERIAL

Supporting Material can be found online at https://doi.org/10.1016/j.bpj.2019.07.006.

AUTHOR CONTRIBUTIONS

B.C. and J.S. conceived of the technique. B.C., B.M., and J.S. designed the experiments in the study. B.C. developed the TPF methodology, performed the optical experiments, and analyzed the data. B.M. designed the DHFR constructs, labeled the samples, and performed the in vitro biochemical assays. B.C., B.M., and J.S. prepared the manuscript. J.S. supervised the research.

SUPPORTING CITATIONS

References (35–41) appear in the Supporting Material.

REFERENCES

1. Shi, Y. 2014. A glimpse of structural biology through X-ray crystallography. *Cell.* 159:995–1014.

2. Marion, D. 2013. An introduction to biological NMR spectroscopy. *Mol. Cell. Proteomics.* 12:3006–3025.

3. Bai, X. C., G. McMullan, and S. H. Scheres. 2015. How cryo-EM is revolutionizing structural biology. *Trends Biochem. Sci.* 40:49–57.

4. Sawaya, M. R., and J. Kraut. 1997. Loop and subdomain movements in the mechanism of *Escherichia coli* dihydrofolate reductase: crystallographic evidence. *Biochemistry.* 36:586–603.

5. Keedy, D. A., H. van den Bedem, …, J. S. Fraser. 2014. Crystal cryo-cooling distorts conformational heterogeneity in a model Michaelis complex of DHFR. *Structure.* 22:899–910.

6. Carriles, R., D. N. Schafer, …, J. A. Squier. 2009. Invited review article: imaging techniques for harmonic and multiphoton absorption fluorescence microscopy. *Rev. Sci. Instrum.* 80:081101.

7. Simpson, G. J., S. G. Westerbuhr, and K. L. Rowlen. 2000. Molecular orientation and angular distribution probed by angle-resolved absorbance and second harmonic generation. *Anal. Chem.* 72:887–898.

8. Yamaguchi, S., H. Hosoi, …, T. Tahara. 2010. Physisorption gives narrower orientational distribution than chemisorption on a glass surface: a polarization-sensitive linear and nonlinear optical study. *J. Phys. Chem. Lett.* 1:2662–2665.

9. Rao, Y., S.-Y. Hong, …, K. B. Eisenthal. 2011. Molecular orientational distribution at interfaces using second harmonic generation. *J. Phys. Chem. C.* 115:11678–11683.

10. Reeve, J. E., A. D. Corbett, …, H. L. Anderson. 2012. Probing the orientational distribution of dyes in membranes through multiphoton microscopy. *Biophys. J.* 103:907–917.

11. Salafsky, J. S. 2007. Second-harmonic generation for studying structural motion of biological molecules in real time and space. *Phys. Chem. Chem. Phys.* 9:5704–5711.

12. Haupert, L. M., and G. J. Simpson. 2009. Chirality in nonlinear optics. *Annu. Rev. Phys. Chem.* 60:345–365.

13. Yan, E. C., Z. Wang, and L. Fu. 2015. Proteins at interfaces probed by chiral vibrational sum frequency generation spectroscopy. *J. Phys. Chem. B.* 119:2769–2785.

14. Heinz, T. F., H. W. K. Tom, and Y. R. Shen. 1983. Determination of molecular orientation of monolayer adsorbates by optical second-harmonic generation. *Phys. Rev. A.* 28:1883–1885.

15. Felderhof, B. U., A. Bratz, …, F. Sieverdes. 1993. Optical second-harmonic generation from adsorbate layers in total-reflection geometry. *J. Opt. Soc. Am.* 10:1824–1833.

16. Brasselet, S. 2011. Polarization-resolved nonlinear microscopy: application to structural molecular and biological imaging. *Adv. Opt. Photonics.* 3:205–271.

17. Moree, B., K. Connell, …, J. Salafsky. 2015. Protein conformational changes are detected and resolved site specifically by second-harmonic generation. *Biophys. J.* 109:806–815.

18. Rajagopalan, P. T., Z. Zhang, …, G. G. Hammes. 2002. Interaction of dihydrofolate reductase with methotrexate: ensemble and single-molecule kinetics. *Proc. Natl. Acad. Sci. USA.* 99:13481–13486.

19. Fierke, C. A., K. A. Johnson, and S. J. Benkovic. 1987. Construction and evaluation of the kinetic scheme associated with dihydrofolate reductase from *Escherichia coli. Biochemistry.* 26:4085–4092.

20. Salafsky, J. S., and K. B. Eisenthal. 2000. Second harmonic spectroscopy: detection and orientation of molecules at a biomembrane interface. *Chem. Phys. Lett.* 319:435–439.

21. Goh, M. C., J. M. Hicks, …, K. Bhattacharyya. 1988. Absolute orientation of water molecules at the neat water surface. *J. Phys. Chem.* 92:5074–5075.

22. Clancy, B., and J. Salafsky. 2017. Second-harmonic phase determination by real-time in situ interferometry. *Phys. Chem. Chem. Phys.* 19:3722–3728.

23. Simpson, G. J., and K. L. Rowlen. 1999. An SHG magic angle: dependence of second harmonic generation orientation measurements on the width of the orientation distribution. *J. Am. Chem. Soc.* 121:2635–2636.

24. Ekhoff, J. A., M. J. Farrow, …, K. L. Rowlen. 2003. Molecular orientation of a model liquid crystal alignment layer. *Talanta.* 60:801–808.

25. Rao, Y., Y.-S. Tao, and H.-F. Wang. 2003. Quantitative analysis of orientational order in the molecular monolayer by surface second harmonic generation. *J. Chem. Phys.* 119:5226–5236.

26. Reyes, V. M., M. R. Sawaya, …, J. Kraut. 1995. Isomorphous crystal structures of *Escherichia coli* dihydrofolate reductase complexed with folate, 5-deazafolate, and 5,10-dideazatetrahydrofolate: mechanistic implications. *Biochemistry.* 34:2710–2723.

27. Radkiewicz, J. L., and C. L. Brooks. 2000. Protein dynamics in enzymatic catalysis: Exploration of dihydrofolate reductase. *J. Am. Chem. Soc.* 122:225–231.

28. Osborne, M. J., J. Schnell, …, P. E. Wright. 2001. Backbone dynamics in dihydrofolate reductase complexes: role of loop flexibility in the catalytic mechanism. *Biochemistry.* 40:9846–9859.

29. Boehr, D. D., J. R. Schnell, …, P. E. Wright. 2013. A distal mutation perturbs dynamic amino acid networks in dihydrofolate reductase. *Biochemistry.* 52:4605–4619.

30. van den Bedem, H., G. Bhabha, …, J. S. Fraser. 2013. Automated identification of functional dynamic contact networks from X-ray crystallography. *Nat. Methods.* 10:896–902.

31. Osborne, M. J., R. P. Venkitakrishnan, …, P. E. Wright. 2003. Diagnostic chemical shift markers for loop conformation and substrate and cofactor binding in dihydrofolate reductase complexes. *Protein Sci.* 12:2230–2238.

32. Venkitakrishnan, R. P., E. Zaborowski, …, P. E. Wright. 2004. Conformational changes in the active site loops of dihydrofolate reductase during the catalytic cycle. *Biochemistry.* 43:16046–16055.

33. Cameron, C. E., and S. J. Benkovic. 1997. Evidence for a functional role of the dynamics of glycine-121 of *Escherichia coli* dihydrofolate reductase obtained from kinetic analysis of a site-directed mutant. *Biochemistry.* 36:15792–15800.

34. Swanwick, R. S., P. J. Shrimpton, and R. K. Allemann. 2004. Pivotal role of Gly 121 in dihydrofolate reductase from *Escherichia coli*: the altered structure of a mutant enzyme may form the basis of its diminished catalytic performance. *Biochemistry.* 43:4119–4127.

35. Heinz, T. F. 1991. Second-order nonlinear optical effects at surfaces and interfaces. *In* Nonlinear Surface Electromagnetic Phenomena. H.-E. Ponath and G. I. Stegeman, eds. Elsevier, pp. 353–416.

36. Simpson, G. J. 2017. Nonlinear Optical Polarization Analysis in Chemistry and Biology. Cambridge University Press.

37. Martin-Fernandez, M. L., C. J. Tynan, and S. E. Webb. 2013. A 'pocket guide' to total internal reflection fluorescence. *J. Microsc.* 252:16–22.

38. Thompson, N. L., H. M. McConnell, and T. P. Burhardt. 1984. Order in supported phospholipid monolayers detected by the dichroism of fluorescence excited with polarized evanescent illumination. *Biophys. J.* 46:739–747.

39. Burghardt, T. P., and N. L. Thompson. 1984. Effect of planar dielectric interfaces on fluorescence emission and detection. Evanescent excitation with high-aperture collection. *Biophys. J.* 46:729–737.

40. Baccanari, D. P., S. Daluge, and R. W. King. 1982. Inhibition of dihydrofolate reductase: effect of NADPH on the selectivity and affinity of diaminobenzylpyrimidines. *Biochemistry.* 21:5068–5075.

41. Boehr, D. D., D. McElheny, …, P. E. Wright. 2010. Millisecond time-scale fluctuations in dihydrofolate reductase are exquisitely sensitive to the bound ligands. *Proc. Natl. Acad. Sci. USA.* 107:1373–1378.